Design and Control of a Midair Reconfigurable Quadcopter using Unactuated Hinges

Nathan Bucki, *Student Member, IEEE,* Jerry Tang, *Student Member, IEEE,* and Mark W. Mueller, *Member, IEEE*

***Abstract*—This paper presents the design and control of a novel quadcopter capable of changing shape mid-flight, allowing for operation in four configurations with the capability of sustained hover in three. The normally rigid connections between the arms of the quadcopter and the central body are replaced by free-rotating hinges that allow the arms to fold downward; no additional actuators beyond the four motors that drive the propellers are used. Configuration transitions are accomplished by either reducing or reversing the thrust forces produced by specific propellers during flight. Constraints placed on the control inputs of the vehicle prevent the arms from folding or unfolding unexpectedly, allowing for the use of existing quadcopter controllers and trajectory generation algorithms. For our experimental vehicle at hover, we find that these constraints result in a 36% reduction of the maximum yaw torque the vehicle can produce, but do not result in a reduction of the maximum thrust or roll and pitch torques. Furthermore, the ability to change configurations is shown to enable the vehicle to traverse small passages, perch on hanging wires, and perform simple grasping tasks.**

***Index Terms*—Aerial Systems: Mechanics and Control, Aerial Systems: Applications, Biologically-Inspired Robots, Reconfigurable Aerial Systems**

I. Introduction

In recent years, quadcopters have proven to be useful in performing a number of tasks such as building inspection, surveillance, package delivery, and search and rescue. Many extensions of the original quadcopter design have been proposed in order to allow for new tasks to be performed, improving their utility. However, this typically requires the vehicle to carry additional hardware, which not only can reduce flight time due to the increased weight of the system, but can also increase the complexity of the vehicle, making it more difficult to build and maintain, which can lead to a higher likelihood of system failures. In this work we present a design change to the quadcopter which allows the vehicle to change shape during flight, perch, and perform simple aerial manipulation, all without requiring significant hardware additions (e.g. motors or complex mechanisms).

A. Related Work

Several aerial vehicles capable of changing shape have been previously developed. For example, in [1] a vehicle capable of automatically unfolding after being launched from tube is presented, and in [2] a vehicle is presented which uses foldable origami-style arms to automatically increase its wingspan during takeoff. Although such designs excel in enabling the rapid deployment of aerial vehicles, they do not focus on repeated changes of shape, and thus require intervention to be returned to their compressed forms.

Vehicles capable of changing shape mid-flight have also been developed in order to enable the traversal of narrow passages. In [3] a vehicle that uses several servomotors to actuate a scissor-like structure that can shrink or expand the size of the vehicle is presented, and in [4] a single servomotor is used in conjunction with an origami structure to enable the arms of a quadcopter to shorten or lengthen during flight. Vehicles that use a central actuator to change the angle of their arms in an X-shape are presented in [5] and [6], and a vehicle that uses four servomotors to change each arm angle is presented in [7] and extended in [8]. In [9] and [10] a quadcopter design is presented that is capable of using one or more actuators to reposition the propellers of the vehicle to be above one another such that the horizontal dimension of the vehicle is reduced. Similarly, [11] uses a single actuator to reposition the propellers of the vehicle to be in a horizontal line, and demonstrates the vehicle being used to traverse a narrow gap.

A large body of work has also been produced regarding the use of quadcopters to perform aerial manipulation. Aerial vehicles with the capability to interact with the environment open the door to a wide range of potential applications, e.g. performing construction as shown in [12]. Typically such designs involve attaching one or more robot arms to a quadcopter, as shown in [13], [14], and [15] for example. Several designs involve changing the structure of the vehicle, such as [7] (described previously) and [16], which describes a ring-shaped multicopter-like vehicle capable of changing the relative position of each propeller such that the body of the vehicle can be used to grasp objects. Other designs, such as [17], use passive elements to engage a gripper and a single actuator to disengage the gripper. However, such designs require the vehicle to carry one or more actuators beyond the four motors used to drive the propellers (e.g. servomotors used for opening/closing a gripper), increasing the weight of the vehicle and therefore decreasing flight time. Additional examples of vehicles used to perform aerial manipulation can be found in the aerial manipulation survey papers [18] and [19].

Finally, several designs have been proposed that enable aerial vehicles to perch on structures in the environment. Such vehicles are able to fly to a desired location, attach themselves to a feature in the environment, and then remain stationary without consuming significant amounts of energy (e.g. while

The authors are with the High Performance Robotics Lab at the University of California, Berkeley, Berkeley, CA, 94709 e-mail: {nathan_bucki, jerrytang, mwm}@berkeley.edu.

monitoring the surrounding area). In [20] a passive adhesive mechanism is proposed for perching on smooth surfaces, and in [21] adhesive pads are used in conjunction with a servomotor to attach and detach the vehicle from vertical walls. In [22] and [23] grippers actuated using servomotors are used to enable perching on bars. Similarly, [24] describes a purely passive gripper that used the weight of the vehicle to close a gripper around a horizontal bar.

In this work, we extend our prior work [25] in several ways, enabling the vehicle to perform several of the previously mentioned tasks while requiring only minor changes to the design and control of the vehicle compared to a conventional quadcopter.

B. Capabilities of the novel vehicle

In [25] a quadcopter design was presented that replaced the typically rigid connections between the arms of the quadcopter and the central body with sprung hinges that allow for the arms of the quadcopter to fold downward when low thrusts are produced by the propellers. This feature enabled the vehicle to reduce its largest dimension while in projectile motion, allowing the vehicle to fly towards a narrow gap, collapse its arms, and then unfold after traversing the gap. In this work we perform two significant design changes. First, we remove the springs used to fold the arms, and instead fold each arm by reversing the thrust direction of the attached propeller. Second, we change the geometry of the vehicle such that when two opposite arms are folded, the thrust vectors of the associated propellers are offset from one another, allowing for a yaw torque to be produced when the thrust direction of the propellers is reversed.

No actuators or complex mechanisms are added to the vehicle, keeping its mass low, and only standard off-the-shelf components (e.g. propellers, motors, and electronic speed controllers) are used in the design, with the exception of the custom 3D printed frame of the vehicle. Thus, the main difference between the vehicle described in this paper and a conventional quadcopter is the fact that each arm is attached to the central body via a rotational joint rather than with a rigid connection.

These changes enable the vehicle to perform a number of tasks as shown in Figure 1, namely:

- Stable flight as a conventional quadcopter with all four arms unfolded
- Stable flight with two arms folded, allowing for the traversal of narrow tunnels
- Grasping of and flight with objects of appropriate dimensions
- Perching on wires with all four arms folded
- Traversal of narrow gaps in projectile motion with all four arms folded

By avoiding the use of complex mechanisms or additional actuators beyond the four motors used to drive the propellers, the proposed vehicle is capable of flying in the unfolded configuration with an efficiency nearly identical to that of a similarly designed conventional quadcopter. The main drawback of our design is the fact that stricter bounds must be placed on the four thrust forces such that the vehicle remains in the desired configuration during flight. However, as we will show in Section IV-C, these bounds do not significantly reduce the agility of the vehicle except in terms of a decrease of the maximum yaw torque the vehicle can produce in the unfolded configuration.

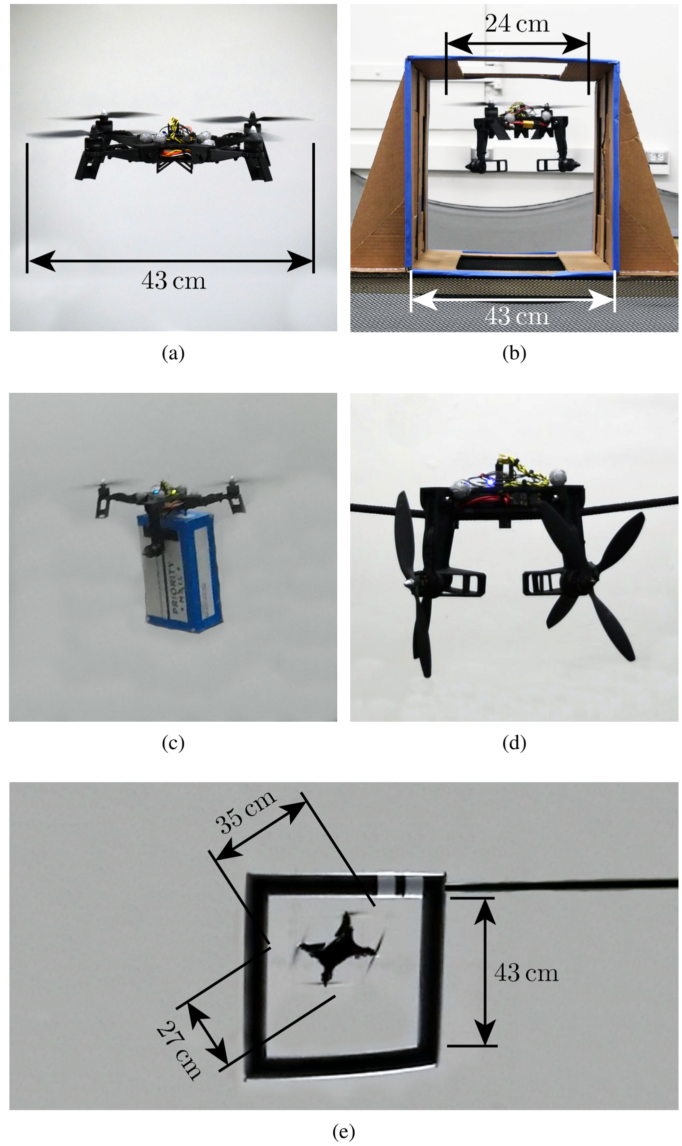

Fig. 1. Images of the experimental vehicle performing a variety of different tasks. The vehicle is capable of flying like a conventional quadcopter when in the unfolded configuration (a), but when flying in the two-arms-folded configuration is able to, e.g., traverse narrow tunnels (b) and perform simple aerial manipulation tasks such as carrying a box (c). Additionally, by allowing all four arms to fold, the vehicle is able to perch on thin wires (d), and even traverse narrow gaps in projectile motion (e) (view from below).

II. System model

In this section we follow [25] in defining a model of the system and deriving the dynamics of the vehicle. The dynamics of the vehicle are then used in Section III to derive bounds on the control inputs such that the vehicle remains in the desired configuration.

The vehicle consists of four rigid arms connected to a central body via unactuated rotary joints (i.e. hinges) which are limited to a range of motion of 90°. Unlike [25], however, each hinge is positioned such that the vehicle is only 180° axis-symmetric rather than 90° axis-symmetric. Figure 2 shows a top-down view of the vehicle, including the orientation of each of the hinges and arms.

A. Notation

Non-bold symbols such as m represent scalars, lowercase bold symbols such as $\boldsymbol{g}$ represent first order tensors (vectors), and uppercase bold symbols such as $\boldsymbol{J}$ represent second order tensors (matrices). Subscripts such as m_B represent the body to which the symbol refers, and superscripts such as $\boldsymbol{g}^E$ represent the frame in which the tensor is expressed. A second subscript or superscript such as $\boldsymbol{\omega}_{BE}$ or $\boldsymbol{R}^{BE}$ represents what the quantity is defined with respect to. The symbol $\boldsymbol{d}$ represents a displacement, $\boldsymbol{\omega}$ represents an angular velocity, and $\boldsymbol{R}$ represents a rotation matrix. The skew-symmetric matrix form of the cross product is written as $\boldsymbol{S}(\boldsymbol{a})$ such that $\boldsymbol{S}(\boldsymbol{a})\,\boldsymbol{b} = \boldsymbol{a} \times \boldsymbol{b}$.

B. Model

The system is modeled as five coupled rigid bodies: the four arms and the central body of the vehicle. The inertial frame is notated as E, the frame fixed to the central body as B, and the frame fixed to arm $i \in \{1,2,3,4\}$ as A_i. The rotation matrix of frame B with respect to frame E is defined as $\boldsymbol{R}^{BE}$ such that the quantity $\boldsymbol{v}^B$ expressed in the B frame is equal to $\boldsymbol{R}^{BE}\boldsymbol{v}^E$ where $\boldsymbol{v}^E$ is the same quantity expressed in frame E. The orientation of arm i with respect to the central body is defined through the single degree of freedom rotation matrix $\boldsymbol{R}^{A_iB}$.

When used in a subscript of a displacement tensor or its time derivatives, E is defined as a fixed point in the inertial frame, B as the center of mass of the central body, and A_i as the center of mass of arm i. For example, $\boldsymbol{d}^B_{A_iB}$ represents the displacement of the center of mass of arm i with respect to the center of mass of the central body, and is expressed in the body-fixed frame B. Furthermore, let P_i be a point along the thrust axis of propeller i, and let H_i be the point where the rotation axis of hinge i intersects with the plane swept by the thrust axis of propeller i as arm i rotates about its hinge.

The internal reaction forces and torques acting at the hinge are defined as $\boldsymbol{f}_{r_i}$ and $\boldsymbol{\tau}_{r_i}$ respectively. The propeller attached to arm i produces scalar thrust force f_{p_i} and aerodynamic reaction torque τ_{p_i} in the $\boldsymbol{z}_{A_i}$ direction. We assume that the torque produced by each propeller is piecewise linearly related to the propeller thrust force [26] with positive proportionality constants $\kappa^+$and κ^-such that:

$$\tau_{p_i} = \begin{cases} (-1)^i \kappa^+ f_{p_i} & f_{p_i} \geq 0 \\ (-1)^i \kappa^- f_{p_i} & f_{p_i} < 0 \end{cases} \tag{1}$$

where $(-1)^i$ models the handedness of the propellers, $f_{p_i} < 0$ when the propellers are spun in reverse, and $\kappa^+ \neq \kappa^-$ when asymmetric propellers are used, as is common with quadcopters.

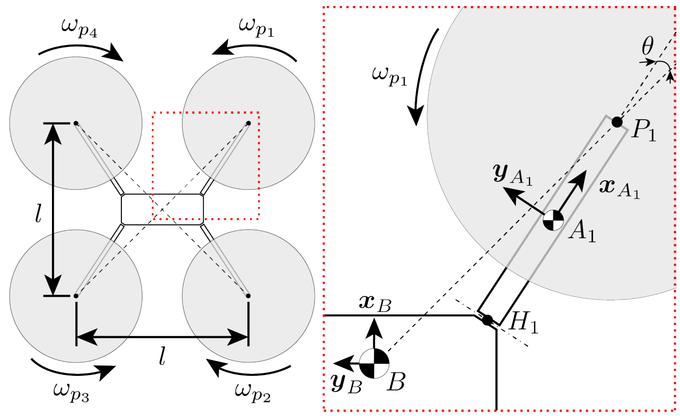

Fig. 2. Top-down view of vehicle in the unfolded configuration (left) and arm A_1 (right). In the unfolded configuration, the thrust axis of each rotor is parallel and equidistant from its neighbor, as is typical for quadcopters. Each arm is connected to the central body by a hinge that rotates in the $\boldsymbol{y}_{A_i}$ direction, allowing the arms to independently rotate between the folded and unfolded configurations. The orientation of each hinge relative to the central body is determined by θ. Each propeller produces a thrust force f_{p_i} and torque τ_{p_i} at P_i in the direction of $\boldsymbol{z}_{A_i}$.

The mass and mass moment of inertia of the central body taken at the center of mass of the central body are denoted m_B and $\boldsymbol{J}_B$ respectively, and the mass and mass moment of inertia arm i taken at its center of mass are denoted m_{A_i} and $\boldsymbol{J}_{A_i}$ respectively.

C. Dynamics

The translational and rotational dynamics of the central body of the vehicle and the four arms are found using Newton's second law and Euler's law respectively [27]. We assume that the only external forces and torques acting on the vehicle are those due to gravity and the thrusts and torques produced by each propeller (for example, aerodynamic effects acting on the central body or arms are not considered). The time derivative of a vector is taken in the reference frame in which that vector is expressed.

We express the translational dynamics of the central body in the inertial frame E, and the rotational dynamics of the central body in the body-fixed frame B. Let $\boldsymbol{g}$ be the acceleration due to gravity. The translational dynamics of the central body are then:

$$m_B \ddot{\boldsymbol{d}}^E_{BE} = m_B \boldsymbol{g}^E + \boldsymbol{R}^{EB} \sum_{i=1}^{4} \boldsymbol{f}^B_{r_i} \tag{2}$$

and the rotational dynamics of the central body are:

$$\begin{aligned} &\boldsymbol{J}^B_B \dot{\boldsymbol{\omega}}^B_{BE} + \boldsymbol{S}\left(\boldsymbol{\omega}^B_{BE}\right) \boldsymbol{J}^B_B \boldsymbol{\omega}^B_{BE} \\ &\qquad = \sum_{i=1}^{4} \left(\boldsymbol{\tau}^B_{r_i} + \boldsymbol{S}\left(\boldsymbol{d}^B_{H_iB}\right) \boldsymbol{f}^B_{r_i}\right) \end{aligned} \tag{3}$$

We express the translational and rotational dynamics of arm i in frame A_i. The translational dynamics of arm i are (note $\boldsymbol{f}^{A_i}_{r_i} = \boldsymbol{R}^{A_iB} \boldsymbol{f}^B_{r_i}$):

$$m_{A_i} \left(\boldsymbol{R}^{A_iE} \ddot{\boldsymbol{d}}^E_{BE} + \boldsymbol{\alpha}\right) = m_{A_i} \boldsymbol{R}^{A_iE} \boldsymbol{g}^E + \boldsymbol{z}^{A_i}_{A_i} f_{p_i} - \boldsymbol{f}^{A_i}_{r_i} \tag{4}$$

where $\boldsymbol{\alpha}$ is

$$\begin{aligned}\boldsymbol{\alpha} =& \boldsymbol{R}^{A_iB}\left(\boldsymbol{S}(\boldsymbol{d}^B_{BH_i})\,\dot{\boldsymbol{\omega}}^B_{BE} + \boldsymbol{S}(\boldsymbol{\omega}^B_{BE})\,\boldsymbol{S}(\boldsymbol{d}^B_{BH_i})\,\boldsymbol{\omega}^B_{BE}\right)\\ &+ \boldsymbol{S}\left(\boldsymbol{d}^{A_i}_{H_iA_i}\right)\dot{\boldsymbol{\omega}}^{A_i}_{A_iE} + \boldsymbol{S}\left(\boldsymbol{\omega}^{A_i}_{A_iE}\right)\boldsymbol{S}\left(\boldsymbol{d}^{A_i}_{H_iA_i}\right)\boldsymbol{\omega}^{A_i}_{A_iE}\end{aligned} \tag{5}$$

The rotational dynamics of arm i are (note $\boldsymbol{\tau}^{A_i}_{r_i} = \boldsymbol{R}^{A_iB}\boldsymbol{\tau}^B_{r_i}$):

$$\begin{aligned}\boldsymbol{J}^{A_i}_{A_i}\dot{\boldsymbol{\omega}}^{A_i}_{A_iE} + \boldsymbol{S}\left(\boldsymbol{\omega}^{A_i}_{A_iE}\right)\boldsymbol{J}^{A_i}_{A_i}\boldsymbol{\omega}^{A_i}_{A_iE} = \boldsymbol{S}\left(\boldsymbol{d}^{A_i}_{P_iA_i}\right)\boldsymbol{z}^{A_i}_{A_i}f_{p_i}\\ + \boldsymbol{z}^{A_i}_{A_i}\tau_{p_i} - \boldsymbol{\tau}^{A_i}_{r_i} - \boldsymbol{S}\left(\boldsymbol{d}^{A_i}_{H_iA_i}\right)\boldsymbol{f}^{A_i}_{r_i}\end{aligned} \tag{6}$$

The equations of motion of the arm are written in terms of $\dot{\boldsymbol{\omega}}^{A_i}_{A_iE}$ and $\boldsymbol{\omega}^{A_i}_{A_iE}$ for convenience, which evaluate to:

$$\begin{aligned}\boldsymbol{\omega}^{A_i}_{A_iE} &= \boldsymbol{\omega}^{A_i}_{A_iB} + \boldsymbol{R}^{A_iB}\boldsymbol{\omega}^B_{BE}\\ \dot{\boldsymbol{\omega}}^{A_i}_{A_iE} &= \dot{\boldsymbol{\omega}}^{A_i}_{A_iB} + \boldsymbol{R}^{A_iB}\dot{\boldsymbol{\omega}}^B_{BE} - \boldsymbol{S}\left(\boldsymbol{\omega}^{A_i}_{A_iB}\right)\boldsymbol{R}^{A_iB}\boldsymbol{\omega}^B_{BE}\end{aligned} \tag{7}$$

Furthermore, note that the reaction torque acting in the rotation direction of hinge i is zero when arm i is rotating between the folded and unfolded configurations ($\boldsymbol{y}^{A_i}_{A_i}\cdot\boldsymbol{\tau}^{A_i}_{r_i} = 0$), positive when arm i is in the folded configuration ($\boldsymbol{y}^{A_i}_{A_i}\cdot\boldsymbol{\tau}^{A_i}_{r_i} \geq 0$), and negative when arm i is in the unfolded configuration ($\boldsymbol{y}^{A_i}_{A_i}\cdot\boldsymbol{\tau}^{A_i}_{r_i} \leq 0$). Thus, in order for arm i to remain in a desired position when starting in that position (i.e. folded or unfolded), the vehicle must be controlled such that $\boldsymbol{y}^{A_i}_{A_i}\cdot\boldsymbol{\tau}^{A_i}_{r_i}$ remains either positive (to remain folded) or negative (to remain unfolded). Such a method is presented in the following section.

III. CONTROL

In this section we describe the controllers used to control the vehicle in each of its configurations. We focus on three distinct configurations: the unfolded configuration (shown in Figure 1a), the two-arms-folded configuration (shown in Figures 1b and 1c), and the four-arms-folded configuration (shown in Figure 1e).

The vehicle is capable of controlled hover in both the unfolded and two-arms-folded configurations. In the unfolded configuration, the vehicle acts as a conventional quadcopter; each of the four propellers produce positive thrust forces ($f_{p_i} > 0$) in the $\boldsymbol{z}_B$ direction. However, in the two-arms-folded configuration, only two propellers of the same handedness produce positive thrust forces in the $\boldsymbol{z}_B$ direction; the other two propellers spin in reverse, producing negative thrust forces that cause their associated arms to fold downward. In this configuration, the folded arms are positioned such that the thrust forces produced by their associated propellers create a yaw torque that counteracts the yaw torque produced by the other two propellers. Note that for the design considered in this paper, the arms have a 90° range of motion such that the thrust produced by a folded arm has no component in the $\boldsymbol{z}_B$ direction.

In the four-arms-folded configuration each of the four propellers are spun in reverse ($f_{p_i} < 0$), resulting in all four arms folding. Although the vehicle is not capable of controlled hover in this configuration, the attitude of the vehicle can still be fully controlled, allowing for the vehicle to reorient itself while in projectile motion.

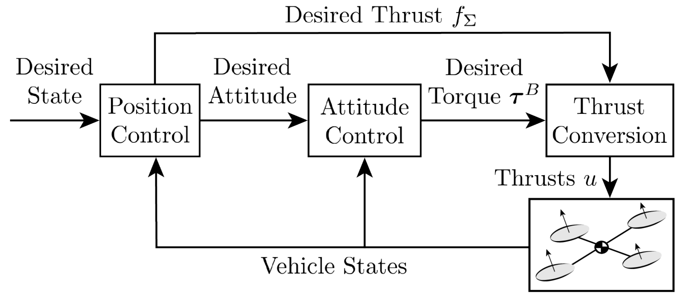

Fig. 3. Cascaded controller used to control the vehicle.

A cascaded control structure typical of multicopter control, shown in Figure 3, is used to control the vehicle in both the unfolded and two-arms-folded configurations. A position controller first computes a desired acceleration based on position and velocity errors, allowing for the computation of the desired total thrust in the $\boldsymbol{z}_B$ direction, f_Σ. Then, an attitude controller computes the desired torque required to align the thrust direction $\boldsymbol{z}_B$ with the desired acceleration direction and achieve the desired yaw angle. Finally, the individual propeller thrust forces necessary to generate the desired total thrust and desired body torque are computed. For each propeller, the desired thrust is converted to a desired angular velocity, which an electronic speed controller is used to track.

A similar control structure is used in the four-arms-folded configuration. However, because the four arms do not produce thrust in the $\boldsymbol{z}_B$ direction while folded, we omit the position controller and instead command desired attitudes to the attitude controller directly. The individual thrust forces that minimize the sum of each thrust force squared while producing the desired torque are then computed. Note these thrust forces can be efficiently computed using the Moore-Penrose pseudoinverse of the matrix relating the four thrust forces to the torque acting on the vehicle.

A. Individual thrust force computation

The individual propeller thrust forces $u = (f_{p_1}, f_{p_2}, f_{p_3}, f_{p_4})$ are related to the desired total thrust in the $\boldsymbol{z}_B$ direction f_Σ and the desired torques about the axes of the body-fixed B frame, $\boldsymbol{\tau}^B = (\tau_x, \tau_y, \tau_z)$ as follows:

$$\begin{bmatrix} f_\Sigma \\ \boldsymbol{\tau}^B \end{bmatrix} = \begin{bmatrix} M_{f_\Sigma} \\ M_{\boldsymbol{\tau}^B} \end{bmatrix} u = Mu \tag{8}$$

where $M_{f_\Sigma} \in \mathbb{R}^{1\times4}$ is the mapping from u to f_Σ, $M_{\boldsymbol{\tau}^B} \in \mathbb{R}^{3\times4}$ is the mapping from u to $\boldsymbol{\tau}^B$, and $M \in \mathbb{R}^{4\times4}$ is the combined mapping.

The mapping M is computed using the geometry of the vehicle and the torque produced by each propeller as a function of the thrust it produces. Let $\boldsymbol{d}_{P_iC}$ be the position of propeller P_i relative to the center of mass of the entire vehicle C, and $\kappa_{p_i} = (-1)^i\kappa^+$ or $\kappa_{p_i} = (-1)^i\kappa^-$ depending on the thrust direction of propeller i as defined in (1). Then, the i-th columns of M_{f_Σ} and $M_{\boldsymbol{\tau}^B}$ are

$$M_{f_\Sigma}[i] = \boldsymbol{z}^B_{A_i}\cdot\boldsymbol{z}^B_B, \quad M_{\boldsymbol{\tau}^B}[i] = \boldsymbol{S}\left(\boldsymbol{d}^B_{P_iC}\right)\boldsymbol{z}^B_{A_i} + \kappa_{p_i}\boldsymbol{z}^B_{A_i} \tag{9}$$

where we recall that $\boldsymbol{z}^B_{A_i}$ is a unit vector written in the body-fixed frame B that points in the positive thrust direction of propeller i.

Thus, in the unfolded configuration, M_u is the mapping of a typical quadcopter with l defined as shown in Figure 2:

$$M_u = \begin{bmatrix} 1 & 1 & 1 & 1 \\ -l/2 & -l/2 & l/2 & l/2 \\ -l/2 & l/2 & l/2 & -l/2 \\ -\kappa^+ & \kappa^+ & -\kappa^+ & \kappa^+ \end{bmatrix} \tag{10}$$

The mapping M_{2f} for the two-arms-folded configuration with arms A_2 and A_4 folded and θ defined as shown in Figure 2 is defined as follows. An equivalent mapping exists for the two-arms-folded configuration with arms A_1 and A_3 folded.

$$\begin{aligned} M_{2f} &= \begin{bmatrix} 1 & 0 & 1 & 0 \\ -l/2 & p_x & l/2 & -p_x \\ -l/2 & -p_y & l/2 & p_y \\ -\kappa^+ & -p_z & -\kappa^+ & -p_z \end{bmatrix} \\ p_x &= d^B_{P_2C,z}\cos(45^\circ+\theta) - \kappa^- \sin(45^\circ+\theta) \\ p_y &= d^B_{P_2C,z}\sin(45^\circ+\theta) + \kappa^- \cos(45^\circ+\theta) \\ p_z &= \frac{l\sqrt{2}}{2}\sin\theta \end{aligned} \tag{11}$$

where we note that the arms are of equal length, i.e. $d^B_{P_1C,z} = d^B_{P_2C,z} = d^B_{P_3C,z} = d^B_{P_4C,z}$.

Finally, the mapping M_{4f} for the four-arms folded configuration is defined as:

$$M_{4f} = \begin{bmatrix} 0 & 0 & 0 & 0 \\ p_x & p_x & -p_x & -p_x \\ p_y & -p_y & -p_y & p_y \\ p_z & -p_z & p_z & -p_z \end{bmatrix} \tag{12}$$

The structure of these mappings can be analyzed to infer how different parameters of the vehicle affect how the vehicle can be controlled in each configuration. For example, we note that when the arms are not angled (i.e. when $\theta = 0$ as was done in our prior work [25]), the term p_z as defined in (11) equals zero. In this case, the vehicle would only be able to produce negative yaw torques due to the fact that the folded arms would be unable to offset the yaw torque produced by the two unfolded arms. Similarly, if $\theta = 0$, the vehicle would be unable to produce any yaw torque in the four-arms-folded configuration as the bottom row of M_{4f} would be zero. However, we observe that (10) does not depend on θ at all, showing that the thrust mapping matrix is unaffected by the choice of arm angle in the unfolded configuration.

Note that, unlike M_u, both M_{2f} and M_{4f} depend on the position of the center of mass of the vehicle in the $\boldsymbol{z}_B$ direction due to the fact that the thrust forces produced by the folded arms are perpendicular to $\boldsymbol{z}_B$. Thus, if the position of the center of mass of the vehicle in the $\boldsymbol{z}_B$ direction is changed (e.g. by adding a payload to the vehicle as shown in Figure 1c), the mappings M_{2f} and M_{4f} must reflect this change.

Furthermore, because the thrust forces of the folded arms are perpendicular to $\boldsymbol{z}_B$, there can exist a nonzero force in the $\boldsymbol{x}_B$ and $\boldsymbol{y}_B$ directions when flying in the two- or four-arms folded configurations. In the two-arms-folded configuration with arms A_2 and A_4 folded, for example, thrusts f_{p_2} and f_{p_4} act in opposite directions such that they produce a force of magnitude $|f_{p_2} - f_{p_4}|$. Because this force is zero at hover and remains small for small τ_x and τ_y (note that $|f_{p_2} - f_{p_4}|$ is not dependent on f_Σ or τ_z due to the structure of M_{2f}), we choose to treat such forces as disturbances in order to maintain the simplicity of the proposed controller.

B. Attitude control

The attitude controller is designed using desired first-order behavior, described here by the rotation vector $\boldsymbol{r} = (\phi_e, \theta_e, \psi_e)$ that represents the rotation between the current and desired attitude (i.e. a rotation about the axis defined in the direction of $\boldsymbol{r}$ by angle $||\boldsymbol{r}||$). Note that, to first order, ϕ_e, θ_e, and ψ_e represent roll, pitch, and yaw respectively. The desired attitude is defined as that attitude at which the yaw angle of the vehicle matches the desired yaw angle and at which the thrust direction of the vehicle matches the desired thrust direction, which is given by the position controller (see Figure 3).

The linearized attitude dynamics of the vehicle are then

$$\begin{bmatrix} \dot{\boldsymbol{r}} \\ \ddot{\boldsymbol{r}} \end{bmatrix} = A \begin{bmatrix} \boldsymbol{r} \\ \dot{\boldsymbol{r}} \end{bmatrix} + B\boldsymbol{\tau}^B \tag{13}$$

where

$$A = \begin{bmatrix} \mathbf{0} & \boldsymbol{I} \\ \mathbf{0} & \mathbf{0} \end{bmatrix}, \quad B = \begin{bmatrix} \mathbf{0} \\ (\boldsymbol{J}^C_C)^{-1} \end{bmatrix} \tag{14}$$

and where $\boldsymbol{J}^C_C$ is the moment of inertia of the entire vehicle written at its center of mass. Note that $\boldsymbol{J}^C_C$ depends on the configuration of the vehicle.

We choose to synthesize an infinite-horizon LQR controller [28] with state cost matrix $Q \in \mathbb{R}^{6\times 6}$ and input cost matrix $R_{\boldsymbol{\tau}^B} \in \mathbb{R}^{3\times 3}$. For each configuration of the vehicle, we weight the cost of each state error independently such that Q is a diagonal matrix. The values of the diagonal of Q are chosen such that the costs associated with ϕ_e and θ_e (i.e. elements 1 and 2) are equal and such that the costs associated with the roll rate and pitch rate (i.e. elements 4 and 5) are equal. However, we choose to define the input cost matrix $R_{\boldsymbol{\tau}^B}$ using the mapping $M_{\boldsymbol{\tau}^B}$ from the individual thrust forces u to the desired torque $\boldsymbol{\tau}^B$ as defined in (8) (i.e. the lower three rows of M_u, M_{2f}, or M_{4f}, depending on the configuration of the vehicle):

$$R_{\boldsymbol{\tau}^B} = (M^+_{\boldsymbol{\tau}^B})^T R_u M^+_{\boldsymbol{\tau}^B} \tag{15}$$

where $M^+_{\boldsymbol{\tau}^B}$ is the pseudoinverse of the mapping matrix $M_{\boldsymbol{\tau}^B}$, and $R_u \in \mathbb{R}^{4\times 4}$ is a diagonal matrix that encodes the cost associated with the thrust force produced by each propeller.

In this work we choose the diagonal entries of R_u based upon whether the associated propeller is spinning in the forward or reverse direction, as the propeller exhibits different characteristics in each mode of operation. For example, conventional propellers produce significantly less thrust when spinning in the reverse direction as they are typically optimized to spin in only the forward direction. Thus, we define $R_u = \mathrm{diag}(r^+, r^+, r^+, r^+)$ for the unfolded configuration,

$R_u = \text{diag}(r^+, r^-, r^+, r^-)$ for the two-arms-folded configuration, and $R_u = \text{diag}(r^-, r^-, r^-, r^-)$ for the four-arms-folded configuration, where r^+ is the cost associated with the propellers spinning in the forward direction, and r^- is the cost associated with the propellers spinning in the reverse direction. In general, $r^+ < r^-$ as conventional quadcopter propellers are optimized to spin in the forward direction.

By defining the input cost matrix $R_{\boldsymbol{\tau}^B}$ as a function of the mapping matrix $M_{\boldsymbol{\tau}^B}$, we can straightforwardly synthesize different infinite-horizon LQR attitude controllers for each configuration of the vehicle. Furthermore, the torque cost matrix $R_{\boldsymbol{\tau}^B}$ can be used to analyze the ability of the vehicle to control its attitude in different configurations, as it describes the cost of producing an arbitrary torque on the vehicle while implicitly accounting for the geometry of the vehicle due to its dependence on $M_{\boldsymbol{\tau}^B}$.

C. Thrust limits

Although the thrust produced by each propeller is already bounded by the performance limitations of the motor driving it, we impose additional bounds which ensure the vehicle remains in the desired configuration. Imposing these bounds ensures that none of the arms begin to fold or unfold unexpectedly, which means the mappings M_u, M_{2f}, and M_{4f} derived in Section III-A will remain valid during flight. Of course, the bounds are not imposed when changing between configurations.

Rather than bounding the individual thrust forces, we choose to instead bound f_Σ and $\boldsymbol{\tau}^B$ using the model derived in Section II. Our approach is similar to that of [25], but differs in its inclusion of the arm angle θ, resulting in a modified expression for the bound.

1) Unfolded configuration bounds: We first note that by enforcing bounds that prevent each arm from folding or unfolding, the vehicle can be treated as one rigid body rather than five coupled rigid bodies. Thus, the acceleration of the center of mass of the vehicle expressed in the inertial frame $\ddot{\boldsymbol{d}}^E_{CE}$ is:

$$\ddot{\boldsymbol{d}}^E_{CE} = \boldsymbol{g}^E + \frac{1}{m_\Sigma}\boldsymbol{R}^{EB}\boldsymbol{z}^B_B f_\Sigma \tag{16}$$

where the total vehicle mass is $m_\Sigma = m_B + 4m_{A_i}$.

Similarly, the angular acceleration of the vehicle can be written as follows, where $\boldsymbol{J}^B_\Sigma$ represents the moment of inertia of the vehicle taken at its center of mass and expressed in the body-fixed frame B. We assume that the angular velocity of the vehicle $\boldsymbol{\omega}^B_{BE}$ is small such that second order terms with respect to $\boldsymbol{\omega}^B_{BE}$ can be neglected (e.g. $\boldsymbol{S}(\boldsymbol{\omega}^B_{BE})\,\boldsymbol{J}^B_\Sigma\boldsymbol{\omega}^B_{BE}$).

$$\dot{\boldsymbol{\omega}}^B_{BE} = \left(\boldsymbol{J}^B_\Sigma\right)^{-1}\boldsymbol{\tau}^B \tag{17}$$

Next, after some algebraic manipulation of (4) and (6) (omitted here for brevity), we find that the reaction torque about hinge i, i.e. $\boldsymbol{y}^{A_i}_{A_i} \cdot \boldsymbol{\tau}^{A_i}_{r_i}$, is linear with respect to $\ddot{\boldsymbol{d}}^E_{CE}$, $\dot{\boldsymbol{\omega}}^B_{BE}$, and propeller thrust f_{p_i}. Recall that f_{p_i} can be computed by inverting the mapping given in (8), meaning that $\ddot{\boldsymbol{d}}^E_{CE}$, $\dot{\boldsymbol{\omega}}^B_{BE}$, and f_{p_i} are all linear functions of f_Σ and $\boldsymbol{\tau}^B$. Thus, we find that the torque about hinge i is also a linear function of f_Σ and $\boldsymbol{\tau}^B$.

As discussed previously, arm i will remain in the unfolded configuration when $\boldsymbol{y}^{A_i}_{A_i}\cdot\boldsymbol{\tau}^{A_i}_{r_i} \le 0$. Therefore, because $\boldsymbol{y}^{A_i}_{A_i}\cdot\boldsymbol{\tau}^{A_i}_{r_i}$ is linear with respect to f_Σ and $\boldsymbol{\tau}^B$, the following four bounds can be computed that ensure each of the four arms remain in the unfolded configuration:

$$c_{f_i} f_\Sigma + c_{x_i}\tau_x + c_{y_i}\tau_y + c_{z_i}\tau_z \ge 0, \quad i \in \{1,2,3,4\} \tag{18}$$

where c_{f_i}, c_{x_i}, c_{y_i}, and c_{z_i} are all constants that depend on the physical attributes of the vehicle.

For the unfolded configuration, the constants in (18) are as follows. Here we have included the assumption that $\boldsymbol{J}^B_\Sigma = \text{diag}(J^B_{\Sigma,xx}, J^B_{\Sigma,yy}, J^B_{\Sigma,zz})$ in order to allow for clearer analysis of c_{x_i}, c_{y_i}, and c_{z_i}. We give the magnitudes of each term, noting that c_{x_i}, c_{y_i}, and c_{z_i} have different signs depending which arm they are associated with.

$$c_{f_i} = \frac{1}{4}d^{A_i}_{P_iH_i,x} - d^{A_i}_{A_iH_i,x}\frac{m_{A_i}}{m_\Sigma} \tag{19}$$

$$|c_{x_i}| = \frac{d^{A_i}_{P_iH_i,x}}{2l} - \frac{\tilde{J}^{A_i}_{A_i,yy}\cos(45^\circ+\theta) + \tilde{m}_A\sin(45^\circ+\theta)}{J^B_{\Sigma,xx}} \tag{20}$$

$$|c_{y_i}| = -\frac{d^{A_i}_{P_iH_i,x}}{2l} + \frac{\tilde{J}^{A_i}_{A_i,yy}\sin(45^\circ+\theta) + \tilde{m}_A\cos(45^\circ+\theta)}{J^B_{\Sigma,yy}} \tag{21}$$

$$|c_{z_i}| = \frac{d^{A_i}_{P_iH_i,x}}{4\kappa^+} - \frac{\tilde{m}_A}{J^B_{\Sigma,zz}} \tag{22}$$

where $\tilde{m}_A$ and $\tilde{J}^{A_i}_{A_i,yy}$ are

$$\tilde{J}^{A_i}_{A_i,yy} = \left(\boldsymbol{J}^{A_i}_{A_i} + m_{A_i}\boldsymbol{S}\left(\boldsymbol{d}^{A_i}_{A_iH_i}\right)\boldsymbol{S}\left(\boldsymbol{d}^{A_1}_{CA_1}\right)\right)_{yy} \tag{23}$$

$$\tilde{m}_A = m_{A_i}d^{A_i}_{A_iH_i,x}d^{A_1}_{CH_1,y} \tag{24}$$

Because of the equal magnitudes of the constants c_{f_i}, c_{x_i}, c_{y_i}, and c_{z_i} in the unfolded configuration, we can aggregate the four bounds given in (18) into a single bound:

$$c_{f_i}f_\Sigma - |c_{x_i}\tau_x| - |c_{y_i}\tau_y| - |c_{z_i}\tau_z| \ge 0 \tag{25}$$

Note that (25) can always be satisfied by increasing f_Σ, as this corresponds to requiring each propeller to produce more thrust (note that in general $c_{f_i} > 0$). By examining (19), we observe that the bound becomes less restrictive when, e.g., the ratio of the mass of an arm to the total mass of the vehicle decreases, as this results in a larger magnitude c_{f_i}. Similarly, because the magnitude of c_{z_i} decreases as κ^+ increases, the bound can be made less restrictive by, e.g., choosing propellers with a larger magnitude κ^+.

Finally, note that by writing this bound as a function of f_Σ and $\boldsymbol{\tau}^B$, we can apply a similar method to that presented in [29] to reduce these control inputs in the event that the bound is not satisfied. Specifically, if the controller presented in the previous subsections produces a f_Σ and $\boldsymbol{\tau}^B$ that does not satisfy (25), we first reduce the magnitude of the yaw torque τ_z until the bound is satisfied or $\tau_z = 0$. Next, if the bound is still not satisfied, we increase f_Σ until the bound is satisfied or it reaches the maximum total thrust the propellers can produce. If the maximum total thrust is reached, then the roll and/or pitch torques are reduced until the bound is satisfied. In practice, however, decreasing the roll and/or pitch torques in order to prevent the arms from folding is seldom necessary due to the magnitude of c_{x_i} and c_{y_i} relative to the other terms.

2) Two- and four-arms-folded configuration bounds: Similar expressions for c_{f_i}, c_{x_i}, c_{y_i}, and c_{z_i} can be found for the two- and four-arms-folded configurations, which we compute using a computer algebra system due to their algebraic complexity (and thus omit here for brevity).[1] Note that no aggregate bound such as (25) exists for the two- or four-arms-folded configuration, and thus it is necessary to enforce each bound given by (18) individually. However, the hierarchical modification of the control inputs f_Σ and $\boldsymbol{\tau}^B$ described previously can still be used to ensure the bounds are satisfied, guaranteeing that the vehicle remains in the desired configuration under the previously stated assumptions.

Numerical values for c_{f_i}, c_{x_i}, c_{y_i}, and c_{z_i} are given in Section IV-C for the experimental vehicle in both the unfolded and two-arms-folded configurations. We do not provide such values for the four-arms-folded configuration, as in practice we have found it to be unnecessary to enforce such bounds. This is because the thrust forces required to transition into the four-arms-folded configuration are typically large enough to prevent the arms from unfolding without the need to enforce additional bounds.

D. Configuration transitions

Next we describe the method used to transition between configurations of the vehicle. We choose to focus on the transitions between the unfolded and two-arms-folded configurations as well as between the unfolded and four-arms-folded configurations, as these are the only transitions required to produce the behaviors of the vehicle demonstrated in this paper. An example of the transition from the unfolded configuration to the two-arms-folded configuration and back is given in Section V-A, and an example of the transition from the unfolded configuration to the four-arms-folded configuration and back is given in Section V-D.

When transitioning between the unfolded and two-arms-folded configurations, we have found it sufficient to instantaneously change between the controller used in the unfolded configuration and the controller used in the two-arms-folded configuration. This discrete change in controllers is largely enabled by the fact that the vehicle possesses significant enough agility in either configuration to recover from small disturbances encountered during the transition. However, the transition is complicated by the fact that the vehicle experiences a significant yaw disturbance during the transition. This yaw disturbance occurs because it is necessary to reverse the rotation direction of two of the propellers of the same handedness during the transition. Specifically, the reversing propellers cannot offset the yaw torque produced by the propellers attached to the unfolded arms, which remain spinning in the forward direction. Additionally, the revering propellers experience a change in angular momentum that results in a corresponding change in angular velocity of the vehicle. Thus, after completing the maneuver, the vehicle will have a significantly different yaw angle and yaw rate than when the maneuver was initiated. In practice, we deal with this difference in yaw angle by choosing the post-transition desired yaw angle such that once the maneuver is completed the yaw error is small.

Unlike the transition to or from the two-arms-folded configuration, the transitions between the unfolded and four-arms-folded configurations are accomplished by commanding constant forward or reverse thrusts while the four arms are moving to the unfolded or folded configurations respectively. After all four arms have finished transitioning, we resume controlling the vehicle using either the unfolded or two-arms-folded controller as appropriate. The period of constant thrusts is required to ensure that all four arms fold or unfold simultaneously, and prevents any attitude errors that would otherwise be introduced by attempting to control the vehicle while the arms are transitioning (as M_u and M_{4f} would not be valid during the transition).

IV. Experimental Vehicle Design

In this section we discuss the design of the experimental vehicle shown in Figure 1. We start by describing how the arm angle was chosen based upon other properties of the vehicle, then discuss how the properties of the chosen powertrain (i.e. the battery, speed controllers, motors, and propellers) affect the vehicle design, and finally discuss how the design of the vehicle influences several important properties of the proposed controllers for each configuration of the vehicle.

The properties of the experimental vehicle are given in Table I. The overall dimensions of the experimental vehicle were chosen to be as similar as possible to a commonly used quadcopter design. Specifically, $8\,\mathrm{in}$ propellers spaced $24\,\mathrm{cm}$ apart are used, which correspond to the same spacing and size of the propellers that would be used with a DJI F330 frame (e.g. as used in [30]). We chose to use commonly available components in the vehicle design to demonstrate its similarity to a conventional quadcopter, and designed the vehicle to have a similar performance (in terms of power consumption and agility) as a conventional quadcopter when flying in the unfolded configuration.

Onboard the vehicle, a Crazyflie 2.0 flight controller is used to run the attitude controller and to transmit individual propeller angular velocity commands to four DYS SN30A electronic speed controllers (ESCs) at 500Hz. The vehicle is powered by a three cell, 40C, $1500\,\mathrm{mA\,h}$ LiPo battery, and four EMAX MT2208 brushless motors are used to drive four Gemfan 8038 propellers.

A motion capture system is used to localize the vehicle, although in principal any sufficiently accurate localization method (e.g. using onboard cameras) could be used. Note that we do not directly measure the position of any individual arm of the vehicle, and instead only measure the position and attitude of the central body of the vehicle. The position and attitude of the vehicle are measured by the motion capture system at 200Hz, and the angular velocity of the vehicle is

[1] We provide code for computing these bounds, as well as performing much of the other analyses and controller syntheses described in this paper, at: https://github.com/nlbucki/MidairReconfigurableQuadcopter

TABLE I
EXPERIMENTAL VEHICLE PARAMETERS

Symbol	Parameter	Value
m_{A_i}	Arm mass	$67\,\mathrm{g}$
m_B	Central body mass	$356\,\mathrm{g}$
m_Σ	Total vehicle mass	$624\,\mathrm{g}$
κ^+	Propeller torque per unit positive thrust	$0.0172\,\mathrm{Nm/N}$
κ^-	Propeller torque per unit negative thrust	$0.038\,\mathrm{Nm/N}$
f_{min}	Minimum thrust per propeller	$-3.4\,\mathrm{N}$
f_{max}	Maximum thrust per propeller	$7.8\,\mathrm{N}$
θ	Arm angle	$11.9°$
l	Distance between adjacent propellers	$24\,\mathrm{cm}$
$\boldsymbol{d}^B_{BH_1}$	Position of central body center of mass relative to hinge 1 (written in B frame)	$\begin{pmatrix}-4.5\,\mathrm{cm}\\7.1\,\mathrm{cm}\\-0.2\,\mathrm{cm}\end{pmatrix}$
$\boldsymbol{d}^{A_i}_{H_iA_i}$	Position of hinge relative to arm center of mass (written in arm frame)	$\begin{pmatrix}-7.6\,\mathrm{cm}\\0\,\mathrm{cm}\\-1.4\,\mathrm{cm}\end{pmatrix}$
$d^{A_i}_{PA_i,x}$	Distance of propeller from arm center of mass	$1.4\,\mathrm{cm}$

measured at 500Hz using an onboard rate gyroscope. The position controller runs on an offboard laptop and sends commands to the vehicle via radio at 50Hz.

A. Choice of arm angle

We choose the angle that each arm makes with the diagonal of the vehicle θ, as shown in Figure 2, such that the vehicle is capable of hovering in the two-arms-folded configuration. That is, the vehicle should be capable of producing a total thrust f_Σ to offset gravity while producing zero torque on the vehicle.

Let the thrust each propeller can produce be bounded by $f_{p_i} \in [f_{\text{min}}, f_{\text{max}}]$, where f_{min} and f_{max} are determined by the physical limits of the powertrain of the vehicle. Note that in our case $f_{\text{min}} < 0$ unlike conventional quadcopters which only allow propellers to spin in the forward direction.

We wish to find θ such that $M_{2f}u = (m_\Sigma g, 0, 0, 0)$ with M_{2f} as given in (11) while satisfying constraints on the thrusts each propeller can produce. As the constraints $\tau_x = \tau_y = 0$ can be trivially satisfied for any choice of θ when $f_{p_1} = f_{p_3}$ and $f_{p_2} = f_{p_4}$, we focus on the constraints on the total thrust f_Σ and yaw torque τ_z:

$$f_{p_1} + f_{p_3} \geq m_\Sigma g \tag{26}$$

$$-\kappa^+ \left(f_{p_1} + f_{p_3}\right) - \frac{l\sqrt{2}}{2} \sin\theta \left(f_{p_2} + f_{p_4}\right) = 0 \tag{27}$$

Thus, the following two inequalities must be satisfied in order for the vehicle to be able to hover with two arms folded:

$$\begin{aligned} \theta &\geq \sin^{-1}\left(\frac{-\kappa^+ m_\Sigma g}{l\sqrt{2} f_{\text{min}}}\right) \\ f_{\text{max}} &\geq \frac{m_\Sigma g}{2} \end{aligned} \tag{28}$$

Because the geometry of the experimental vehicle is defined such that an increase in θ corresponds to an increase in the minimum dimension d of the vehicle in the two-arms-folded configuration as shown in Figure 4, we choose the smallest θ such that the vehicle has sufficient control authority to produce reasonable magnitude thrusts and torques with two arms folded. Specifically, we choose

$$\theta = \sin^{-1}\left(\frac{-\kappa^+ m_\Sigma g}{l\sqrt{2} f_{\text{des}}}\right) \tag{29}$$

where $f_{\text{des}} > f_{\text{min}}$ is the nominal thrust force produced by each of the two folded arms during hover. We choose f_{des} to be roughly half f_{min} (recall $f_{\text{min}} < 0$) so that the vehicle is capable of producing roughly equal magnitude yaw torques in each direction.

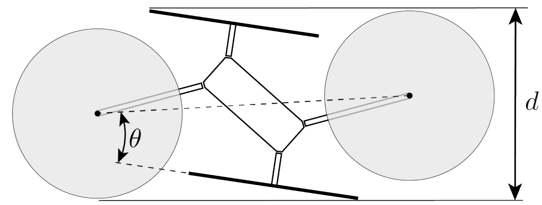

Fig. 4. Top-down view of the vehicle in the two-arms-folded configuration. The minimum horizontal dimension of the vehicle d increases as the arm angle θ increases.

Note that the bound presented in (28) is also dependent on several other parameters of the vehicle. For example, if a smaller θ is desired, it is advantageous to minimize both the mass of the vehicle m_Σ and the coefficient κ^+ that relates the thrust produced by each propeller to the torque acting about its rotation axis. Coincidentally, minimizing these quantities is equivalent to minimizing the power consumption of the vehicle at hover, which is typically a preeminent concern when designing aerial vehicles. Thus, no significant trade-off exists between the power consumption of the vehicle and the choice of θ.

B. Powertrain selection

As discussed in the previous subsection, the arm angle θ is dependent on both the torque per unit positive thrust produced by each propeller κ^+ as well as the maximum magnitude thrust each propeller can produce when spinning in reverse f_{min}. Thus, in order to minimize θ, the ratio between κ^+ and f_{min} must be minimized. To this end, the powertrain (i.e. battery, speed controllers, motors, and propellers) is chosen such that θ is minimized while simultaneously minimizing the power consumption of the vehicle while flying in the unfolded configuration, as this would likely be the primary mode of operation of the vehicle. In our model, f_{min} and f_{max} are determined by the design of the powertrain, and κ^+ and κ^- are determined by the chosen propellers.

Although we spin several of the propellers in the reverse direction in the two- or four-arms-folded configurations, this does not imply that it would necessarily be advantageous to use symmetric propellers (sometimes referred to as "3D propellers") which are designed to spin in both directions. When compared to conventional propellers, symmetric propellers have the advantage of being able to produce much larger thrusts when spinning in reverse (i.e. f_{min} is larger in

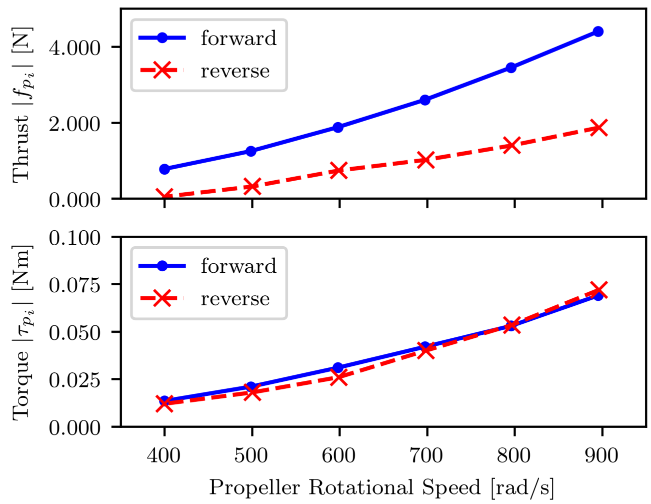

Fig. 5. Magnitude of thrust and torque produced by an 8038 propeller spinning in both the forward and reverse directions. A load cell capable of measuring forces and torques was used in conjunction with an optical tachometer to collect the data. The propeller produces significantly more thrust but produces roughly the same magnitude torque when spinning in the forward direction compared to the reverse direction for a given speed.

magnitude), but this comes at the cost of a smaller maximum forward thrust $f_{\max}$ and a larger torque per unit positive thrust κ^+. Thus, it is possible that the use of symmetric propellers may lead to a larger required θ if the ratio of κ^+ to $f_{\min}$ is larger than that of a conventional propeller. Additionally, $f_{\max}$ must still be large enough to satisfy the constraint given in (28), which may be difficult to achieve using symmetric propellers. Finally, the use of symmetric propellers would greatly increase the power consumption of the vehicle when hovering in the unfolded configuration, as symmetric propellers are not optimized to minimize power consumption compared to conventional propellers.

To this end, we choose to use conventional quadcopter propellers on the experimental vehicle. Figure 5 shows how the thrust and torque produced by a Gemfan 8038 propeller are related to the rotational speed of the propeller, demonstrating the difference in thrust produced by the propeller when spinning in the forward and reverse directions. We found that the powertrain of the experimental vehicle was capable of driving the propeller to produce up to 3.4 N of thrust in the reverse direction and 7.8 N of thrust in the forward direction with $\kappa^+ = 0.0172\,\mathrm{Nm/N}$ and $\kappa^- = 0.038\,\mathrm{Nm/N}$. This lead to a choice of $\theta = 11.9°$ according to (29) with $f_{\text{des}} = 1.5\,\mathrm{N}$.

Finally, we note that although in theory f_{p_i} can achieve any value between $f_{\min}$ and $f_{\max}$, in practice we restrict f_{p_i} to not pass through zero unless the vehicle is performing a configuration transition that requires reversing the propeller. This is due to the fact that we use commonly available electronic speed controllers and brushless motors which use back-EMF to sense the speed of the motor. The use of back-EMF to sense motor speed results in significantly degraded performance when changing directions, meaning that such motors are typically restricted to spin in only one direction. Although this property can affect the performance of the proposed vehicle when changing between configurations, once the propellers have reversed direction they can continue to operate without any significant change in performance. Thus, in practice we restrict the thrust forces of propellers spinning in the forward direction and reverse direction to be in $[0, f_{\max}]$ and $[f_{\min}, 0]$ respectively, and only allow the propellers to change direction when changing between configurations.

C. Vehicle Agility

We now examine the effects of the bounds described in Section III-C on the experimental vehicle with thrust limits $f_{\min}$ and $f_{\max}$. For notational convenience, we define $W \in \mathbb{R}^{4\times 4}$ as a matrix with each column defined by $c_{f_i}, c_{x_i}, c_{y_i}$, and c_{z_i} respectively. Then, the bounds defined in (18) can be rewritten as:

$$W \begin{bmatrix} f_\Sigma \\ \boldsymbol{\tau}^B \end{bmatrix} \succeq \mathbf{0} \tag{30}$$

where $\succeq$ denotes an element-wise inequality, and $\mathbf{0}$ denotes a vector of zeros.

Then, the matrix W_u for the experimental vehicle in the unfolded configuration is computed to be the following, where the first column has units of meters and the other columns are unitless.

$$W_u = \begin{bmatrix} 0.0144 & -0.0421 & -0.0252 & -1.304 \\ 0.0144 & -0.0421 & 0.0252 & 1.304 \\ 0.0144 & 0.0421 & 0.0252 & -1.304 \\ 0.0144 & 0.0421 & -0.0252 & 1.304 \end{bmatrix} \tag{31}$$

Similarly, the matrix W_{2f} for the experimental vehicle in the two-arms-folded configuration is computed to be:

$$W_{2f} = \begin{bmatrix} 0.0369 & 0.08 & 0.0225 & 0.0059 \\ 0.0237 & 0.345 & -0.289 & 1.26 \\ 0.0369 & -0.08 & -0.0225 & 0.0059 \\ 0.0237 & -0.345 & 0.289 & 1.26 \end{bmatrix} \tag{32}$$

The individual thrust limits of each propeller can be written in terms of f_Σ and $\boldsymbol{\tau}^B$ by utilizing the inverse of the mapping matrix M introduced in (8):

$$\begin{bmatrix} \boldsymbol{I} \\ -\boldsymbol{I} \end{bmatrix} M^{-1} \begin{bmatrix} f_\Sigma \\ \boldsymbol{\tau}^B \end{bmatrix} \succeq \begin{bmatrix} \mathbf{1} f_{\min} \\ -\mathbf{1} f_{\max} \end{bmatrix} \tag{33}$$

where $\boldsymbol{I}$ the 4×4 identity matrix, and $\mathbf{1}$ is vector of ones of length four.

In order to compare the agility of the experimental vehicle to a conventional quadcopter, we examine how the set of feasible values of f_Σ and $\boldsymbol{\tau}^B$ is reduced when imposing the bounds given in (30) (i.e. those that prevent the arms from folding or unfolding). Note that both the experimental vehicle and a conventional quadcopter must satisfy the bounds on f_Σ and $\boldsymbol{\tau}^B$ given by (33) (i.e. those that ensure $f_{p_i} \in [f_{\min}, f_{\max}]$), but that the experimental vehicle must additionally satisfy the bounds that prevent the arms from folding or unfolding.

The reduction in agility of the experimental vehicle when $\tau_x = \tau_y = 0$ is shown in Figure 6, where we observe how the set of feasible yaw torques τ_z and total thrusts f_Σ is reduced in comparison to a conventional quadcopter. As shown in the figure, the bounds that prevent the arms from folding primarily result in a reduction in the range of

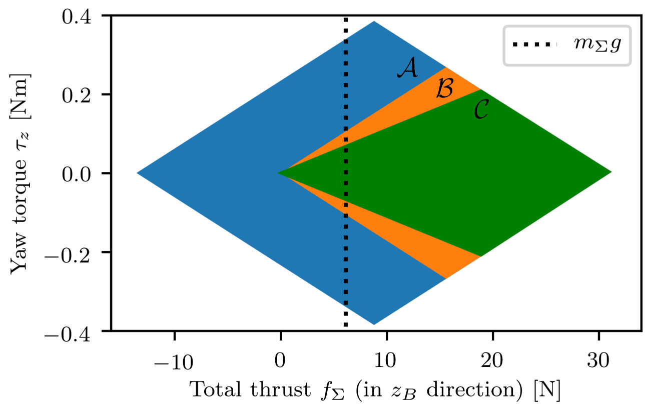

Fig. 6. Range of feasible total thrusts f_Σ and yaw torques τ_z for the experimental vehicle in the unfolded configuration with zero roll and pitch torques $\tau_x = \tau_y = 0$. The dotted black line denotes the value of f_Σ at hover. The blue set $\mathcal{A}$ represents the feasible inputs when only the constraints on the minimum and maximum thrusts of each propeller $f_{\min}$ and $f_{\max}$ are considered. The orange set $\mathcal{B}$ represents the feasible inputs for a conventional quadcopter, i.e. with $f_{\min} = 0$ rather than $f_{\min} < 0$. Finally, the green set $\mathcal{C}$ represents the feasible inputs when the constraints that prevent the arms from folding are imposed, primarily reducing the range of feasible yaw torques. Note that $\mathcal{C} \subset \mathcal{B} \subset \mathcal{A}$.

feasible yaw torques. Specifically, the maximum yaw torque the experimental vehicle can produce at hover (i.e. when $f_\Sigma = m_\Sigma g$ and $\tau_x = \tau_y = 0$) is reduced by 36% when compared to a conventional quadcopter. We note that this is a significant improvement from our previous work [25], where the maximum yaw torque was reduced by roughly 75% when compared to a conventional quadcopter due to the use of springs to fold the arms rather than reverse thrust as we use in this work.

A similar analysis of the maximum magnitude roll and pitch torques the vehicle can produce at hover shows them to be no less than those of a conventional quadcopter, indicating that the bounds that prevent the arms from folding given in (30) are actually less restrictive than those on each of the individual thrust forces given in (33). Finally, we find that the minimum and maximum total thrust forces are also no less than those of a conventional quadcopter, which is also an improved result from our previous work [25] where we found that the minimum total thrust force was 70% of the thrust force required to hover (again due to the use of springs to fold the arms). Thus, this analysis implies that the only significant tradeoff between the proposed vehicle design and a conventional quadcopter (in terms of the control authority of the vehicle) is the reduction of the maximum yaw torque the vehicle can produce.

V. Experimental Results

In this section, we demonstrate how the ability of the proposed vehicle to fold and unfold each arm enables it to perform a number of tasks which would be difficult or impossible to perform using a conventional quadcopter. We first show how the ability to fold two arms of the vehicle enables the vehicle to fly horizontally through narrow tunnels

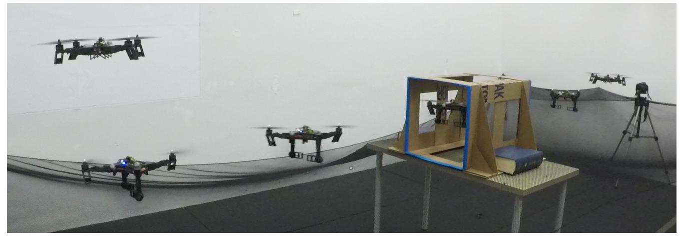

Fig. 7. Composite image of the vehicle transitioning from the unfolded to two-arms-folded configuration (left), flying through a narrow tunnel, and transitioning back to the unfolded configuration (right).

and perform simple aerial grasping, and then demonstrate how all four arms of the vehicle can be folded to perform perching and more aggressive vertical flight through narrow gaps.[2]

A. Horizontal flight through a narrow tunnel

We first demonstrate how the proposed vehicle can be used to fly in confined spaces which would normally be inaccessible to a conventional quadcopter of similar size. The vehicle was flown through a tunnel with a cross section that measures $43\,\mathrm{cm}$ by $43\,\mathrm{cm}$, as shown in Figure 1b. These dimensions were chosen such that the vehicle could not traverse the tunnel in the unfolded configuration even with perfect trajectory tracking, as the minimum width of the vehicle in the unfolded configuration is $43\,\mathrm{cm}$. However, the minimum width of the vehicle in the two-arms-folded configuration is $24\,\mathrm{cm}$, allowing it to pass.

To perform the maneuver, the vehicle first transitions from the unfolded configuration to two-arms-folded configuration, then flies through the tunnel, and finally transitions back to the unfolded configuration as shown in Figure 7. The yaw angle of the vehicle was chosen to maximize the distance of the vehicle from the walls of the tunnel when flying through its center.

B. Grasping

Next, we show how the two-arms-folded configuration can be used to perform a simple grasping task, as shown in Figure 8. In this experiment a box with a mass of $83\,\mathrm{g}$ that measures $9\,\mathrm{cm} \times 15\,\mathrm{cm} \times 25\,\mathrm{cm}$ in height is used. The box was specifically chosen to be $9\,\mathrm{cm}$ in width in order to allow for the box to be grasped without significantly changing the geometry of the two-arms-folded configuration, as the distance between the legs of two opposing folded arms is approximately $9\,\mathrm{cm}$. Note that because the total mass of the vehicle m_Σ increases when holding the box, each of the bounds given in (28) that govern the ability of the vehicle to hover in the two-arms-folded configuration become more restrictive, significantly limiting the maximum mass of a box that can be carried.

The experiment was conducted as follows: The vehicle was first commanded to land on top of the box, which was

[2] Videos of each of the experiments discussed in this section can be viewed in the attached video or at https://youtu.be/xEg8GXlb82g

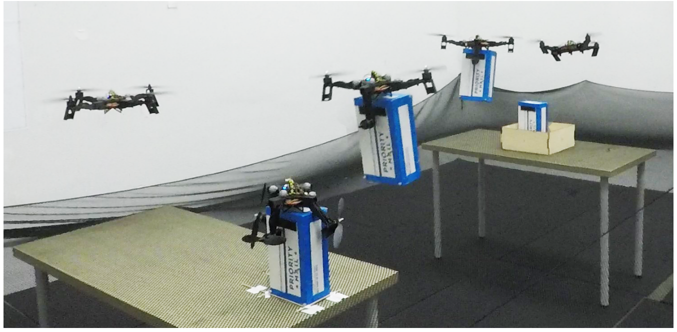

Fig. 8. Composite image of the vehicle grasping a box (left), flying it to a new location, and dropping the box by returning to the unfolded configuration (right).

constrained such that it could not rotate in the yaw direction. After landing, all four propellers were disabled, allowing two of the arms of the vehicle to fall into grasping position. Next, the two arms used to grasp the box were commanded to produce a thrust of $-2\,\mathrm{N}$ for one second to allow the arms to settle into a firm grasping position, after which time the two unfolded arms were commanded to produce a small thrust of $1\,\mathrm{N}$ for one second such that they fully unfolded before takeoff. After this grasping procedure was completed, the vehicle was commanded to takeoff and fly to the desired drop-off location using the two-arms-folded configuration controller, which was modified to account for the change in location of the center of mass of the vehicle as discussed in Section III-A. After flying to the drop-off location, the vehicle was commanded to transition back to the unfolded configuration, resulting the the box being released at the desired location.

C. Wire perching

The vehicle is also capable of perching on wires in the four-arms-folded configuration, as shown in Figure 1d. To perform this maneuver, the vehicle simply aligns itself with the wire and lands on top of it, turning off all four motors when the maneuver is complete. The body of the experimental vehicle includes a notch that runs the length of the central body the vehicle, which helps align the vehicle with the wire when perching. Because only the central body of the vehicle is supported by the wire, the four arms fold downward. This shifts the center of mass of the vehicle below the wire, which allows the vehicle to perch on the wire in a stable configuration. For the experimental vehicle, the center of mass is shifted $4\,\mathrm{cm}$ downward by folding the arms, resulting in the center of mass of the vehicle being $2\,\mathrm{cm}$ below where the wire contacts the vehicle.

D. Vertical flight through a narrow gap

Finally, we demonstrate capability of the vehicle to fold all four arms during flight, allowing for passage through narrow gaps in projectile motion. The maneuver is inspired in part by how birds fold their wings when passing through narrow gaps, as shown in [31], and mirrors our previous work [25], where we demonstrated a similar capability using springs to fold the arms rather than reverse thrust forces. Here we only show the vehicle traversing a gap vertically, as the traversal of gaps in the horizontal direction can be accomplished using the two-arms folded method demonstrated in Section V-A. The gap measures $43\,\mathrm{cm}$ by $43\,\mathrm{cm}$, and the experimental vehicle measures $27\,\mathrm{cm}$ by $35\,\mathrm{cm}$ in the four-arms-folded configuration.

Figure 9 shows images of the gap traversal maneuver, and Figure 10 graphs the trajectory of the vehicle during the maneuver, which consists of the following stages. First, the vehicle aligns itself with the gap while hovering above it. Once aligned, the vehicle begins to accelerate upward from time $t_0 = 0.2\,\mathrm{s}$ to time $t_1 = 0.46\,\mathrm{s}$. After completing this upward trajectory, a constant thrust command of $-1\,\mathrm{N}$ is sent to each propeller at time t_1. At time $t_2 = 0.84\,\mathrm{s}$ the arms finish the transition to the folded configuration, and the four-arms-folded attitude controller is used to stabilize the vehicle, where the desired attitude is chosen such that $\boldsymbol{z}_B$ is in the vertical direction. Next, at time $t_3 = 0.96\,\mathrm{s}$, a constant thrust command of $1\,\mathrm{N}$ is sent to each propeller in order to unfold the arms. The vehicle traverses the gap (located at $3.3\,\mathrm{m}$ in this experiment) at approximately this time. Then, at time $t_4 = 1.21\,\mathrm{s}$, the arms finish unfolding as evidenced by a sharp increase in the acceleration of the vehicle in the $\boldsymbol{z}_B$ direction. At this time the unfolded configuration controller is once again enabled, and the vehicle is commanded to produce a large vertical acceleration until the vertical speed of the vehicle is reduced to zero, which occurs at time $t_5 = 1.51\,\mathrm{s}$.

Note that although using larger constant thrust commands than $1\,\mathrm{N}$ to fold and unfold the arms would result in the arms folding/unfolding more quickly, in practice we have found it preferable to command smaller constant thrust values. This is due to the fact that the arms may not fold at exactly the same time (e.g. due to friction), and thus large constant thrusts may result in large torques being exerted on the vehicle, leading to potentially large attitude errors once the transition is completed. The reduction of attitude errors in the four-arms-folded configuration is crucial because it ensures that the thrust direction of the vehicle will be in the opposite direction of its velocity after transitioning back to the unfolded configuration, allowing for the vehicle to quickly reduce its speed.

VI. Conclusion

In this paper we have presented a novel quadcopter design that differs from a conventional quadcopter in the use of passive hinges which allow each of the four arms to rotate freely between unfolded and folded configurations. The vehicle was designed to be nearly identical to a conventional quadcopter aside from the presence of the four passive hinges, which are lightweight and thus do not significantly affect the power consumption of the vehicle. Although these additional unactuated degrees of freedom require stricter bounds on the thrust forces produced by each propeller, these additional bounds were shown to not significantly affect the agility of the vehicle when flying in the unfolded configuration, aside from a reduced ability to produce yaw torques. Additionally, a method for easily synthesizing controllers for the different

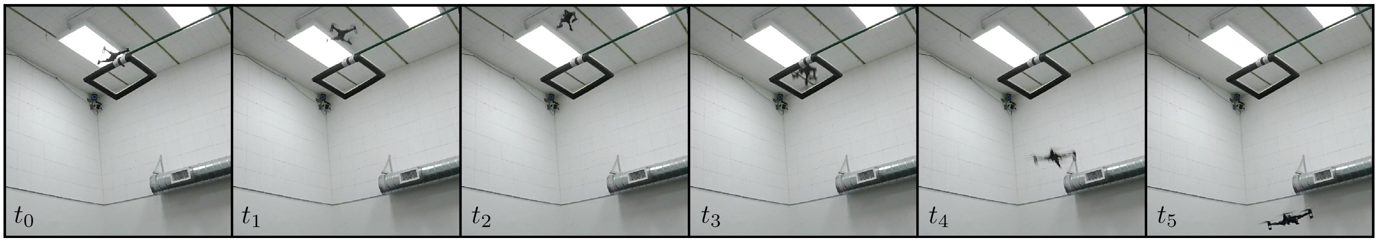

Fig. 9. Image sequence of the vehicle transitioning from the unfolded to the four-arms-folded configuration and back in order to traverse a narrow gap. Data associated with this experiment is shown in Figure 10.

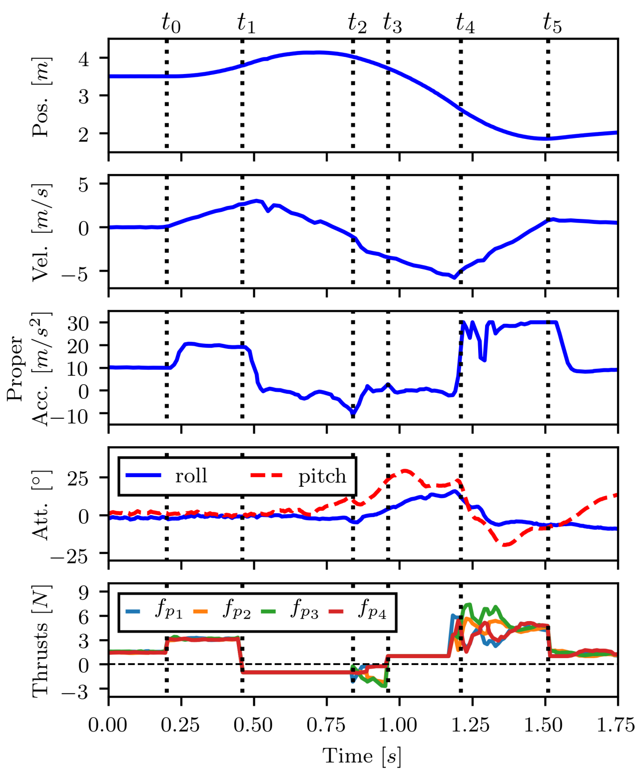

Fig. 10. Trajectory of the vehicle while passing downward through a narrow gap in the four-arms-folded configuration. The position and velocity of the vehicle are given in the vertical $\boldsymbol{z}_E$ direction as measured by the motion capture system, and the proper acceleration is given in the $\boldsymbol{z}_B$ direction as measured by the onboard accelerometer. The vehicle starts accelerating upward at time t_0, and commands each propeller to produce a constant negative thrust at time t_1, initiating the transition to the four-arms-folded configuration. At time t_2 the arms finish folding, and the four-arms-folded controller is used to stabilize the attitude of the vehicle. Next, at time t_3, a constant positive thrust command is sent to each motor to initiate the transition back to the unfolded configuration, resulting in the vehicle returning to the unfolded configuration at time t_4. Finally, the vehicle is commanded to accelerate upward to reduce its downward velocity until the vehicle comes to rest at time t_5.

configurations of the vehicle was presented and used to control the attitude of the vehicle in both the two- and four-arms-folded configurations.

The design of the vehicle was also analyzed based upon the ability of the vehicle to hover in the two-arms-folded configuration. Specifically, it was shown that the angle of the arms relative to the central body is bounded from below by a function of the characteristics of the propellers and the mass and size of the vehicle. This lower bound, however, is structured such that it becomes less strict as the power consumption of the vehicle in the unfolded configuration is reduced, meaning that no tradeoff exists between vehicle power consumption and arm angle. A simple characterization of a conventional quadcopter propeller was also performed, showing that although significantly less thrust is produced by the propeller when spinning in reverse, such propellers can produce enough reverse thrust to enable the vehicle to be controlled in the two-arms-folded configuration with a reasonably small arm angle.

Finally, the viability of the design was demonstrated by constructing an experimental vehicle using commonly available quadcopter components (e.g. standard propellers, motors, etc.), which was shown to be capable of performing a number of tasks that a conventional quadcopter could not perform.

ACKNOWLEDGEMENT

This material is based upon work supported by the National Science Foundation Graduate Research Fellowship under Grant No. DGE 1752814 and by the Berkeley Fellowship for Graduate Study. The experimental testbed at the HiPeRLab is the result of contributions of many people, a full list of which can be found at hiperlab.berkeley.edu/members/.

REFERENCES

[1] A. Bouman, P. Nadan, M. Anderson, D. Pastor, J. Izraelevitz, J. Burdick, and B. Kennedy, "Design and autonomous stabilization of a ballistically-launched multirotor," in *2020 IEEE International Conference on Robotics and Automation (ICRA)*. IEEE, 2020, pp. 8511–8517.

[2] S. Mintchev, L. Daler, G. L'Eplattenier, L. Saint-Raymond, and D. Floreano, "Foldable and self-deployable pocket sized quadrotor," in *2015 IEEE International Conference on Robotics and Automation (ICRA)*. IEEE, 2015, pp. 2190–2195.

[3] N. Zhao, Y. Luo, H. Deng, and Y. Shen, "The deformable quadrotor: Design, kinematics and dynamics characterization, and flight performance validation," in *2017 IEEE/RSJ International Conference on Intelligent Robots and Systems (IROS)*. IEEE, 2017, pp. 2391–2396.

[4] D. Yang, S. Mishra, D. M. Aukes, and W. Zhang, "Design, planning, and control of an origami-inspired foldable quadrotor," in *2019 American Control Conference (ACC)*. IEEE, 2019, pp. 2551–2556.

[5] A. Desbiez, F. Expert, M. Boyron, J. Diperi, S. Viollet, and F. Ruffier, "X-morf: A crash-separable quadrotor that morfs its x-geometry in flight," in *2017 Workshop on Research, Education and Development of Unmanned Aerial Systems (RED-UAS)*. IEEE, 2017, pp. 222–227.

[6] Y. Bai and S. Gururajan, "Evaluation of a baseline controller for autonomous figure-8 flights of a morphing geometry quadcopter: Flight performance," *Drones*, vol. 3, no. 3, p. 70, 2019.

[7] D. Falanga, K. Kleber, S. Mintchev, D. Floreano, and D. Scaramuzza, "The foldable drone: A morphing quadrotor that can squeeze and fly," *IEEE Robotics and Automation Letters*, vol. 4, no. 2, pp. 209–216, 2018.

[8] A. Fabris, K. Kleber, D. Falanga, and D. Scaramuzza, "Geometry-aware compensation scheme for morphing drones," *arXiv preprint arXiv:2003.03929*, 2020.

[9] G. O. Vargas, C. Hintz, L. R. G. Carrillo, F. M. Palacios, and E. S. E. Quesada, "Dynamic modeling of a multi-rotorcraft uas with morphing capabilities," in *2015 International Conference on Unmanned Aircraft Systems (ICUAS)*. IEEE, 2015, pp. 963–971.

[10] A. Sakaguchi, T. Takimoto, and T. Ushio, "A novel quadcopter with a tilting frame using parallel link mechanism," in *2019 International Conference on Unmanned Aircraft Systems (ICUAS)*. IEEE, 2019, pp. 674–683.

[11] V. Riviere, A. Manecy, and S. Viollet, "Agile robotic fliers: A morphing-based approach," *soft robotics*, vol. 5, no. 5, pp. 541–553, 2018.

[12] Q. Lindsey, D. Mellinger, and V. Kumar, "Construction with quadrotor teams," *Autonomous Robots*, vol. 33, no. 3, pp. 323–336, 2012.

[13] J. Thomas, J. Polin, K. Sreenath, and V. Kumar, "Avian-inspired grasping for quadrotor micro uavs," in *ASME 2013 international design engineering technical conferences and computers and information in engineering conference*. American Society of Mechanical Engineers Digital Collection, 2013.

[14] M. Orsag, C. Korpela, M. Pekala, and P. Oh, "Stability control in aerial manipulation," in *2013 American Control Conference*. IEEE, 2013, pp. 5581–5586.

[15] C. Korpela, M. Orsag, and P. Oh, "Towards valve turning using a dual-arm aerial manipulator," in *2014 IEEE/RSJ International Conference on Intelligent Robots and Systems*. IEEE, 2014, pp. 3411–3416.

[16] T. Anzai, M. Zhao, S. Nozawa, F. Shi, K. Okada, and M. Inaba, "Aerial grasping based on shape adaptive transformation by halo: horizontal plane transformable aerial robot with closed-loop multilinks structure," in *2018 IEEE International Conference on Robotics and Automation (ICRA)*. IEEE, 2018, pp. 6990–6996.

[17] D. Mellinger, Q. Lindsey, M. Shomin, and V. Kumar, "Design, modeling, estimation and control for aerial grasping and manipulation," in *2011 IEEE/RSJ International Conference on Intelligent Robots and Systems*. IEEE, 2011, pp. 2668–2673.

[18] X. Meng, Y. He, and J. Han, "Survey on aerial manipulator: System, modeling, and control," *Robotica*, pp. 1–30.

[19] H. B. Khamseh, F. Janabi-Sharifi, and A. Abdessameud, "Aerial manipulationa literature survey," *Robotics and Autonomous Systems*, vol. 107, pp. 221–235, 2018.

[20] E. W. Hawkes, D. L. Christensen, E. V. Eason, M. A. Estrada, M. Heverly, E. Hilgemann, H. Jiang, M. T. Pope, A. Parness, and M. R. Cutkosky, "Dynamic surface grasping with directional adhesion," in *2013 IEEE/RSJ International Conference on Intelligent Robots and Systems*. IEEE, 2013, pp. 5487–5493.

[21] A. Kalantari, K. Mahajan, D. Ruffatto, and M. Spenko, "Autonomous perching and take-off on vertical walls for a quadrotor micro air vehicle," in *2015 IEEE International Conference on Robotics and Automation (ICRA)*. IEEE, 2015, pp. 4669–4674.

[22] K. M. Popek, M. S. Johannes, K. C. Wolfe, R. A. Hegeman, J. M. Hatch, J. L. Moore, K. D. Katyal, B. Y. Yeh, and R. J. Bamberger, "Autonomous grasping robotic aerial system for perching (agrasp)," in *2018 IEEE/RSJ International Conference on Intelligent Robots and Systems (IROS)*. IEEE, 2018, pp. 1–9.

[23] K. Hang, X. Lyu, H. Song, J. A. Stork, A. M. Dollar, D. Kragic, and F. Zhang, "Perching and restinga paradigm for uav maneuvering with modularized landing gears," *Science Robotics*, vol. 4, no. 28, p. eaau6637, 2019.

[24] C. E. Doyle, J. J. Bird, T. A. Isom, J. C. Kallman, D. F. Bareiss, D. J. Dunlop, R. J. King, J. J. Abbott, and M. A. Minor, "An avian-inspired passive mechanism for quadrotor perching," *IEEE/ASME Transactions On Mechatronics*, vol. 18, no. 2, pp. 506–517, 2012.

[25] N. Bucki and M. W. Mueller, "Design and control of a passively morphing quadcopter," in *IEEE International Conference on Robotics and Automation (ICRA)*. IEEE, 2019, pp. 9116–9122.

[26] P. Pounds, R. Mahony, P. Hynes, and J. M. Roberts, "Design of a four-rotor aerial robot," in *Proceedings of the 2002 Australasian Conference on Robotics and Automation (ACRA 2002)*. Australian Robotics & Automation Association, 2002, pp. 145–150.

[27] P. H. Zipfel, *Modeling and Simulation of Aerospace Vehicle Dynamics*, 2nd ed. American Institute of Aeronautics and Astronautics, 2007.

[28] B. Anderson and J. Moore, *Optimal Control: Linear Quadratic Methods*. Prentice-Hall International, 1989.

[29] M. Faessler, D. Falanga, and D. Scaramuzza, "Thrust mixing, saturation, and body-rate control for accurate aggressive quadrotor flight," *IEEE Robotics and Automation Letters*, vol. 2, no. 2, pp. 476–482, 2017.

[30] N. Bucki and M. W. Mueller, "A novel multicopter with improved torque disturbance rejection through added angular momentum," *International Journal of Intelligent Robotics and Applications*, vol. 3, no. 2, pp. 131–143, 2019.

[31] I. Schiffner, H. D. Vo, P. S. Bhagavatula, and M. V. Srinivasan, "Minding the gap: in-flight body awareness in birds," *Frontiers in zoology*, vol. 11, no. 1, p. 64, 2014.